VII International Conference on Computational Methods for Coupled Problems in Science and Engineering
COUPLED PROBLEMS 2017
M. Papadrakakis, E. Oñate and B. Schrefler (Eds)

A STABLE AND EFFICIENT DOMAIN DECOMPOSITION METHOD FOR MAXWELL'S EQUATIONS WITH UNCERTAINTY

ANNA NISSEN*, PER PETTERSSON† AND SVENN TVEIT†

*Department of Mathematics, University of Bergen
P.O.Box 7803, NO-5020 Bergen, Norway
e-mail: anna.nissen@math.uib.no

†Uni Research CIPR
P.O.Box 7800, NO-5020 Bergen, Norway
e-mail: per.pettersson@uni.no, svenn.tveit@uni.no

Key words: Maxwell's Equations, Domain Decomposition, Summation-by-parts Operators, Finite Difference Methods, Generalized Polynomial Chaos

Abstract. Geophysical monitoring of CO_2 sequestration using electromagnetics is prone to large uncertainties. To include uncertainty in Maxwell's equations, we use the polynomial chaos framework and project the equations onto stochastic basis functions. The resulting extended system needs to be solved only once to obtain all statistics of interest. We use high-order finite-difference methods that satisfy a summation-by-parts rule for the spatial discretization of Maxwell's equations. We incorporate spatial adaptivity by decomposing the spatial domain into structured grid blocks, where the discretization of each block is adapted to the local resolution requirement. The spatial discretization is time-stable by a carefully designed numerical coupling between grid blocks of different grid sizes. The combination of spatial adaptivity and high-order finite difference methods on block-structured grids leads to a highly efficient and accurate numerical discretization.

1 INTRODUCTION

Fast and accurate solutions of Maxwell's equations are required to simulate responses in various electromagnetic (EM) applications, e.g., medical and geophysical imaging [1, 2]. In this paper, we are interested in calculating EM responses for time-lapse monitoring of CO_2 sequestration [3] – a geophysical inverse problem.

In geophysical monitoring surveys with EM, signals are transmitted to a subsurface reservoir where they are affected by the subsurface conductivity distribution. The returning signals are measured by surface receivers and converted to a map of the subsurface

conductivity using an inversion method. By incorporating the updated conductivity values from the monitoring survey into a detailed geological description, empirical relations between conductivity and saturation can be used to get updated information on the CO_2 migration path.

To understand and evaluate the risk factors involved in CO_2 storage operations, quantification of uncertainty is very important. In order to solve geophysical monitoring inverse problems, one relies on calculating EM responses using numerical methods. Most often, uncertainty is quantified using Monte Carlo (or sampling-based) algorithms, where the numerical EM simulator is treated as a 'black box' needed to be run many times to achieve sufficiently accurate statistics [4]. Alternatively, uncertainty can be incorporated directly in Maxwell's equations by representing the solution as a spectral expansion in random variables using the generalized polynomial chaos (gPC) framework [5, 6]. Through stochastic Galerkin projection of the problem, repetitive sampling can be completely avoided by solving a single extended system only once.

A large variety of numerical methods exist for solving Maxwell's equations with the finite element (FE), finite difference (FD), and integral equation methods [7, 8]. The most common approaches are FE and FD. In FE methods, discretization of the computational domain is highly flexible using unstructured grids. Hence, complex geometrical features can more easily be captured compared with other methods [9]. However, specialized grid generation software is often required to generate shape regular unstructured grids. Furthermore, special care is needed when solving the resulting FE linear system due to its unstructured nature. On the other hand, FD methods are simple to implement and computationally efficient, due to the resulting linear system being sparse and structured [10]. A challenge of FD methods on structured grids is to handle large computational domains with features on different spatial scales, from sources and receivers on the order of meters to geological features on the order of kilometers. Typically, a fine grid is needed around sources and receivers to obtain highly accurate solutions, while in the far-field, low resolution is sufficient and a coarser grid can be employed.

In this paper, we solve the time-domain, first-order coupled stochastic Galerkin Maxwell's equations using FD methods within the summation-by-parts (SBP) framework, see [11] and references therein. The SBP framework is well suited for designing high-order accurate discretizations that are provably time-stable. In this context, time-stability refers to the property that the growth of numerical errors is bounded, and that a consistent spatial discretization converges to the true solution. In general, proving stability for high-order FD methods is a non-trivial task, in particular for non-uniform grids. A time-stable domain decomposition method based on SBP operators for block-wise spatial adaptivity was developed in [12]. To obtain sufficient resolution for the most important features in the computational domain, we present a numerical discretization that extends the method presented in [12] to the stochastic Galerkin Maxwell's equations. The performance of the method is demonstrated both in the deterministic and the stochastic settings, with geophysical inverse modeling in mind.

2 GENERALIZED POLYNOMIAL CHAOS EXPANSION

In the gPC framework stochastic functions are represented as Fourier series expansions in a set of independent random variables. Assuming a single source of uncertainty the uncertainty of the problem is parameterized by introducing a random variable ξ with known probability measure $\mathcal{P}$. The measure $\mathcal{P}$ could match an estimated empirical distribution of some uncertain input variable, but also be taken as some well-known probability distribution. Next introduce a set of basis functions $\{\psi_i(\xi)\}_{i=1}^{\infty}$ consisting of polynomials that are orthonormal with respect to the measure $\mathcal{P}$, i.e.,

$$\mathbb{E}\left(\psi_i(\xi)\psi_j(\xi)\right) \equiv \int_{-\infty}^{\infty} \psi_i(\xi)\psi_j(\xi)d\mathcal{P}(\xi) = \delta_{ij}.$$

The orthonormal polynomials correspond to classical orthogonal polynomials for some commonly used probability distributions, e.g., Legendre polynomials for uniform distributions and Hermite polynomials for Gaussian distributions. Any function f of finite variance can be approximated by its truncated gPC expansion [6],

$$f \approx \sum_{m=1}^{P} f_m \psi_m(\xi), \tag{1}$$

where the gPC coefficients f_m are defined by the projections

$$f_m = \mathbb{E}(f\psi_m), \quad m = 1, ..., P.$$

The series expansion (1) converges in the L_2 sense as $P \to \infty$. Statistics may be computed directly from the gPC coefficients, e.g., mean and variance are approximated by

$$\mathbb{E}(f) = f_1, \quad \mathrm{Var}(f) = \sum_{m=2}^{P} f_m^2.$$

The extension to multiple independent stochastic dimensions is performed through tensorization of univariate basis functions but not considered in this work.

3 MAXWELL'S EQUATIONS IN TIME DOMAIN

Consider a general spatial domain Ω and temporal domain $t \in [0, T]$. Let $E = (E_x, E_y, E_z)^T$ denote the electric field, $H = (H_x, H_y, H_z)^T$ the magnetic field, ϵ the permittivity, σ the electric conductivity, and μ the magnetic permeability. The three-dimensional Maxwell's equations in the time domain for $(x, y, z) \in \Omega, t \in [0, T]$, are given by

$$\begin{aligned} \epsilon\tfrac{\partial E}{\partial t} - \nabla \times H + \sigma E &= 0, \\ \mu\tfrac{\partial H}{\partial t} + \nabla \times E &= 0, \\ \nabla \cdot E &= 0, \\ \nabla \cdot H &= 0, \end{aligned} \tag{2}$$

with appropriate boundary conditions. Consider a transverse electric wave propagating in the x-y plane. Then (2) simplifies to the two-dimensional hyperbolic system

$$\begin{bmatrix} \epsilon E_x \\ \epsilon E_y \\ \mu H_z \end{bmatrix}_t + \begin{bmatrix} 0 & 0 & 0 \\ 0 & 0 & 1 \\ 0 & 1 & 0 \end{bmatrix} \begin{bmatrix} E_x \\ E_y \\ H_z \end{bmatrix}_x + \begin{bmatrix} 0 & 0 & -1 \\ 0 & 0 & 0 \\ -1 & 0 & 0 \end{bmatrix} \begin{bmatrix} E_x \\ E_y \\ H_z \end{bmatrix}_y + \begin{bmatrix} \sigma & 0 & 0 \\ 0 & \sigma & 0 \\ 0 & 0 & 0 \end{bmatrix} \begin{bmatrix} E_x \\ E_y \\ H_z \end{bmatrix} = 0, \quad (3)$$

where we assume a spatial domain $(x, y) \in \Omega = [0, L_x] \times [0, L_y]$.

3.1 Stochastic Galerkin projection of Maxwell's equations

In geophysical inverse problems, σ is the main source of uncertainty [8], and in the numerical experiments we consider uncertainty in σ only. For completeness we present the problem setup with uncertainty in all material parameters. The field variables E_x, E_y, H_z and any uncertain parameters (ϵ, μ, σ) are expressed as truncated gPC expansions (1) and inserted into the equations (3). A stochastic Galerkin projection onto the basis functions is performed by multiplying the system of equations by each basis function and then integrating with respect to the probability measure $\mathcal{P}$. For projection onto P basis functions, this results in a coupled $3P \times 3P$ system,

$$\underbrace{\begin{bmatrix} \mathbf{A}(\epsilon) & \mathbf{0} & \mathbf{0} \\ \mathbf{0} & \mathbf{A}(\epsilon) & \mathbf{0} \\ \mathbf{0} & \mathbf{0} & \mathbf{A}(\mu) \end{bmatrix}}_{\mathbf{M}} \begin{bmatrix} \mathbf{E}_x \\ \mathbf{E}_y \\ \mathbf{H}_z \end{bmatrix}_t + \underbrace{\begin{bmatrix} \mathbf{0} & \mathbf{0} & \mathbf{0} \\ \mathbf{0} & \mathbf{0} & \mathbf{I} \\ \mathbf{0} & \mathbf{I} & \mathbf{0} \end{bmatrix}}_{\mathbf{B}} \begin{bmatrix} \mathbf{E}_x \\ \mathbf{E}_y \\ \mathbf{H}_z \end{bmatrix}_x + \underbrace{\begin{bmatrix} \mathbf{0} & \mathbf{0} & -\mathbf{I} \\ \mathbf{0} & \mathbf{0} & \mathbf{0} \\ -\mathbf{I} & \mathbf{0} & \mathbf{0} \end{bmatrix}}_{\mathbf{C}} \begin{bmatrix} \mathbf{E}_x \\ \mathbf{E}_y \\ \mathbf{H}_z \end{bmatrix}_y + \underbrace{\begin{bmatrix} \mathbf{A}(\sigma) & \mathbf{0} & \mathbf{0} \\ \mathbf{0} & \mathbf{A}(\sigma) & \mathbf{0} \\ \mathbf{0} & \mathbf{0} & \mathbf{0} \end{bmatrix}}_{\mathbf{D}} \begin{bmatrix} \mathbf{E}_x \\ \mathbf{E}_y \\ \mathbf{H}_z \end{bmatrix} = \mathbf{0}, \quad (4)$$

where we have introduced the matrix $\mathbf{A}(\cdot)$, defined by

$$[\mathbf{A}(r)]_{ij} = \sum_{m=1}^{P} r_m \mathbb{E}(\psi_i \psi_j \psi_m), \quad r = \epsilon, \mu, \sigma.$$

Note that the matrix $\mathbf{A}(\cdot)$ is symmetric, so the matrices $\mathbf{M}, \mathbf{B}, \mathbf{C}$ and $\mathbf{D}$ are also all symmetric. Let $\mathbf{u} = \begin{pmatrix} \mathbf{E}_x & \mathbf{E}_y & \mathbf{H}_z \end{pmatrix}^\mathsf{T}$. We express the system (4) as

$$\mathbf{M}\mathbf{u}_t + \mathbf{B}\mathbf{u}_x + \mathbf{C}\mathbf{u}_y + \mathbf{D}\mathbf{u} = \mathbf{0}. \quad (5)$$

To assign boundary conditions, we use the eigenvalue decompositions of the matrices $\mathbf{B}$ and $\mathbf{C}$,

$$\mathbf{B} = \mathbf{V}_\mathbf{B}^+ \mathbf{\Lambda}_\mathbf{B}^+ \mathbf{V}_\mathbf{B}^{+\mathsf{T}} + \mathbf{V}_\mathbf{B}^- \mathbf{\Lambda}_\mathbf{B}^- \mathbf{V}_\mathbf{B}^{-\mathsf{T}}, \qquad \mathbf{C} = \mathbf{V}_\mathbf{C}^+ \mathbf{\Lambda}_\mathbf{C}^+ \mathbf{V}_\mathbf{C}^{+\mathsf{T}} + \mathbf{V}_\mathbf{C}^- \mathbf{\Lambda}_\mathbf{C}^- \mathbf{V}_\mathbf{C}^{-\mathsf{T}},$$

where superscript $+$ $(-)$ denote the matrices of positive (negative) eigenvalues, $\mathbf{\Lambda}$, and the corresponding eigenvectors, $\mathbf{V}$, respectively. We use the following Dirichlet type boundary conditions

$$\mathbf{V}_\mathbf{B}^{+\mathsf{T}} \mathbf{u} = \mathbf{g}_\mathrm{w}(y,t) \quad \text{at } x = 0, \qquad \mathbf{V}_\mathbf{B}^{-\mathsf{T}} \mathbf{u} = \mathbf{g}_\mathrm{e}(y,t) \quad \text{at } x = L_x,$$
$$\mathbf{V}_\mathbf{C}^{+\mathsf{T}} \mathbf{u} = \mathbf{g}_\mathrm{s}(x,t) \quad \text{at } y = 0, \qquad \mathbf{V}_\mathbf{C}^{-\mathsf{T}} \mathbf{u} = \mathbf{g}_\mathrm{n}(x,t) \quad \text{at } y = L_y,$$

where we use the cardinal directions west (w), east (e), south (s), and north (n) to denote the four boundaries of the computational domain. This choice of boundary conditions leads to a well posed problem (5).

4 NUMERICAL DISCRETIZATION

The stochastic Galerkin Maxwell's equations are discretized with an FD method with an SBP property that allows proof of time-stability for the semi-discrete problem with appropriate boundary conditions [13]. The boundary conditions are enforced to the accuracy order of the scheme through a simultaneous approximation term (SAT) that penalizes the deviation from the exact boundary conditions [14]. By relaxing the condition of exactly satisfying the boundary conditions, we gain flexibility in the formulation that is needed to choose penalty parameters that lead to stability. SBP operators were introduced for the first derivative in [13, 15]. A numerical method based on SBP operators for the deterministic Maxwell's equations with a material discontinuity interface was presented in [16].

In order to be able to resolve point sources and receivers in an extensive computational domain, we decompose the domain into a number of blocks, where the grid sizes can vary between the blocks, see Figures 2(a)-2(c). The SBP-SAT framework is employed to achieve stable and accurate couplings also between the subdomains of different spatial resolution, similar to the treatment of boundary conditions. Due to limited space we have omitted the stability proofs for the discretizations presented in this work.

A fourth-order Runge-Kutta method is used for the temporal integration. The choice of a sufficiently small time-step in combination with high order of accuracy of the time integration leads to a numerical scheme where the error is dominated by the spatial discretization. The spatial error convergence is the focus of this work.

4.1 Spatial discretization of a single domain

We first consider the case of a single domain, i.e., a uniform discretization over the whole domain, and the implementation of boundary conditions. The spatial domain $[0, L_x] \times [0, L_y]$ is discretized at points (x_i, y_j), $i = 1, ..., m_x$, $j = 1, ..., m_y$, and $\Delta x = L_x/(m_x - 1)$, $\Delta y = L_y/(m_y - 1)$. The semi-discrete numerical approximation of $\mathbf{u}(x_i, y_j, t)$ is denoted $\mathbf{v}_{i,j}$ $(= \mathbf{v}_{i,j}(t))$ and assembled in the vector $\mathbf{v} = (\mathbf{v}_{1,1}, ..., \mathbf{v}_{1,m_y}, ..., \mathbf{v}_{m_x,1}, ..., \mathbf{v}_{m_x,m_y})^\intercal$.

In one spatial dimension the first derivative $\mathbf{u}_x$ is approximated by $\mathbf{P}_x^{-1}\mathbf{Q}_x\mathbf{v}$, where $\mathbf{P}_x$ is a positive definite diagonal matrix, scales with Δx, and defines a matrix norm. The matrix $\mathbf{Q}_x$ satisfies

$$\mathbf{Q}_x + \mathbf{Q}_x^\intercal = diag(-1, 0, \ldots, 0, 1) = \mathbf{e}_{m_x}\mathbf{e}_{m_x}^\intercal - \mathbf{e}_1\mathbf{e}_1^\intercal, \tag{6}$$

with $\mathbf{e}_{m_x} = (0, \ldots, 0, 1)^\intercal$ and $\mathbf{e}_1 = (1, 0, \ldots, 0)^\intercal$. The SBP property (6) mimics the semi-discrete (discrete in space, continuous in time) counterpart of integration by parts. This is essential in the derivation of discrete energy estimates to prove time-stability. Operators of accuracy order $2n$, $n \in \mathbb{N}$, in the interior of the domain are combined with boundary stencils of order of accuracy n. In this paper we use fourth-order accurate operators ($n = 2$) from [15].

The Kronecker product notation $\otimes$ is used for extension to more than one spatial dimension and to include the stochastic Galerkin system. The SBP operators can then be handled dimension by dimension. In the following operator subscripts are omitted, as the order of appearance is always (x, y, ξ). Note that size and scaling of $\mathbf{P}$, $\mathbf{Q}$, and $\mathbf{I}$ vary depending on dimension.

In two spatial dimensions, consider the semi-discretization of (5)

$$(\mathbf{I} \otimes \mathbf{I} \otimes \mathbf{M})\mathbf{v}_t + (\mathbf{P}^{-1}\mathbf{Q} \otimes \mathbf{I} \otimes \mathbf{B})\mathbf{v} + (\mathbf{I} \otimes \mathbf{P}^{-1}\mathbf{Q} \otimes \mathbf{C})\mathbf{v} + (\mathbf{I} \otimes \mathbf{I} \otimes \mathbf{D})\mathbf{v} = \text{SAT},$$

where the SAT contributions enforce the boundary conditions and are given by

$$\begin{aligned}\text{SAT} = \tau_{\text{w}}(\mathbf{P}^{-1}\mathbf{e}_1\mathbf{e}_1^\intercal \otimes \mathbf{I} \otimes \mathbf{\Sigma}_{\text{w}}) \left[(\mathbf{I} \otimes \mathbf{I} \otimes \mathbf{V}_{\mathbf{B}}^{+\intercal})\mathbf{v} - \mathbf{g}_{\text{w}})\right] + \tau_{\text{e}}(\mathbf{P}^{-1}\mathbf{e}_{m_x}\mathbf{e}_{m_x}^\intercal \otimes \mathbf{I} \otimes \mathbf{\Sigma}_{\text{e}}) \\ \times \left[(\mathbf{I} \otimes \mathbf{I} \otimes \mathbf{V}_{\mathbf{B}}^{-\intercal})\mathbf{v} - \mathbf{g}_{\text{e}})\right] + \tau_{\text{s}}(\mathbf{I} \otimes \mathbf{P}^{-1}\mathbf{e}_1\mathbf{e}_1^\intercal \otimes \mathbf{\Sigma}_{\text{s}}) \left[(\mathbf{I} \otimes \mathbf{I} \otimes \mathbf{V}_{\mathbf{C}}^{+\intercal})\mathbf{v} - \mathbf{g}_{\text{s}})\right] \\ + \tau_{\text{n}}(\mathbf{I} \otimes \mathbf{P}^{-1}\mathbf{e}_{m_y}\mathbf{e}_{m_y}^\intercal \otimes \mathbf{\Sigma}_{\text{n}}) \left[(\mathbf{I} \otimes \mathbf{I} \otimes \mathbf{V}_{\mathbf{C}}^{-\intercal})\mathbf{v} - \mathbf{g}_{\text{n}})\right].\end{aligned}$$

A stable numerical scheme is obtained by setting the design parameter values to

$$\begin{aligned}&\tau_{\text{w}} = -1, && \tau_{\text{e}} = 1, && \tau_{\text{s}} = -1, && \tau_{\text{n}} = 1, \\ &\mathbf{\Sigma}_{\text{w}} = \mathbf{V}_{\mathbf{B}}^{+}\mathbf{\Lambda}_{\mathbf{B}}^{+}, && \mathbf{\Sigma}_{\text{e}} = \mathbf{V}_{\mathbf{B}}^{-}\mathbf{\Lambda}_{\mathbf{B}}^{-}, && \mathbf{\Sigma}_{\text{s}} = \mathbf{V}_{\mathbf{C}}^{+}\mathbf{\Lambda}_{\mathbf{C}}^{+}, && \mathbf{\Sigma}_{\text{n}} = \mathbf{V}_{\mathbf{C}}^{-}\mathbf{\Lambda}_{\mathbf{C}}^{-}.\end{aligned}$$

4.2 Domain with blocks and T-junction interfaces

In a multi-block setting, single domain discretization operators are used on each block, and the blocks are coupled through numerical interfaces using SAT. Grid block interfaces with different grid sizes are treated with SBP interpolation operators [17] in combination with SAT. When constructing complex block-structured grids so called T-junction interfaces can help to reduce the number of numerical interfaces needed to obtain a stable discretization. This is advantageous because the one-sided FD stencils near interfaces are of lower order of accuracy compared to the interior stencil. A T-junction interface in the vertical direction is shown in Figure 1(a). A grid refinement ratio of $2:1$ is depicted between the left and the right subdomains in Figure 1(b), and this is what we consider in the numerical experiments.

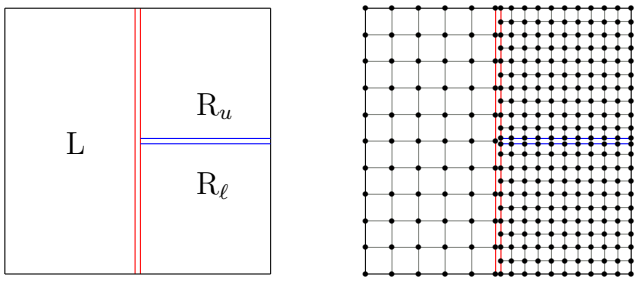

Figure 1: T-junction interface used to obtain a stable discretization on a domain-decomposed grid. The blue lines denote numerical SBP-SAT interfaces between equal grid-size blocks, and red lines interfaces between blocks with different grid sizes. Grid points of two adjacent blocks are co-located at the interface.

Let $\mathbf{v}^{\text{L}}$ be the numerical solution in the left subdomain and $\mathbf{v}^{\text{R}_u}$ and $\mathbf{v}^{\text{R}_\ell}$ denote the numerical solutions in the right upper and lower subdomains, respectively. Further, let $\mathbf{I}_{\text{R}_u\text{R}_\ell}^{\text{L}}$ be an operator that interpolates the solutions on the interface of the right subdomains to the solution on the interface of the left subdomain, and therefore of size $m_y^{\text{L}} \times (m_y^{\text{R}_u} + m_y^{\text{R}_\ell})$. Let $\mathbf{I}_{\text{L}}^{\text{R}_u}$ and $\mathbf{I}_{\text{L}}^{\text{R}_\ell}$ be operators of sizes $m_y^{\text{R}_u} \times m_y^{\text{L}}$ and $m_y^{\text{R}_\ell} \times m_y^{\text{L}}$ that interpolate from the left subdomain to the right upper and lower subdomains. In the case of equal grid sizes, $\mathbf{I}_{\text{R}_u\text{R}_\ell}^{\text{L}}$, $\mathbf{I}_{\text{L}}^{\text{R}_u}$, and $\mathbf{I}_{\text{L}}^{\text{R}_\ell}$ will mainly be identity matrices (with one extra row or column due to duplicate nodes at the T-junction),

except for a few rows and columns around the T-junction. The T-junction operators can be found in [12], and the SBP interpolation operators in [17]. The discretization of (5) for the three blocks in Figure 1 including the coupling of the left domain with the two right domains (double red lines) and the coupling of the two right domains (double blue lines) is given by

$$
\begin{aligned}
&(\mathbf{I}\otimes\mathbf{I}\otimes\mathbf{M})\mathbf{v}_t^{\mathrm{L}} + (\mathbf{P}_{\mathrm{L}}^{-1}\mathbf{Q}_{\mathrm{L}}\otimes\mathbf{I}\otimes\mathbf{B})\mathbf{v}^{\mathrm{L}} + (\mathbf{I}\otimes\mathbf{P}_{\mathrm{L}}^{-1}\mathbf{Q}_{\mathrm{L}}\otimes\mathbf{C})\mathbf{v}^{\mathrm{L}} + (\mathbf{I}\otimes\mathbf{I}\otimes\mathbf{D})\mathbf{v}^{\mathrm{L}} \\
&= \tau_{\mathrm{L}}(\mathbf{P}_{\mathrm{L}}^{-1}\otimes\mathbf{I}\otimes\boldsymbol{\Sigma}_{\mathrm{L}}^{\tau})\left[(\mathbf{e}_{m_x}^{\mathrm{L}}(\mathbf{e}_{m_x}^{\mathrm{L}})^{\intercal}\otimes\mathbf{I}\otimes\mathbf{I})\mathbf{v}^{\mathrm{L}} - (\mathbf{e}_{m_x}^{\mathrm{L}}\otimes\mathbf{I}_{\mathrm{R}_u\mathrm{R}_\ell}^{\mathrm{L}}\otimes\mathbf{I})\begin{bmatrix}((\mathbf{e}_1^{\mathrm{R}_u})^{\intercal}\otimes\mathbf{I}\otimes\mathbf{I})\mathbf{v}^{\mathrm{R}_u}\\((\mathbf{e}_1^{\mathrm{R}_\ell})^{\intercal}\otimes\mathbf{I}\otimes\mathbf{I})\mathbf{v}^{\mathrm{R}_\ell}\end{bmatrix}\right],
\end{aligned}
$$

$$
\begin{aligned}
&(\mathbf{I}\otimes\mathbf{I}\otimes\mathbf{M})\mathbf{v}_t^{\mathrm{R}_u} + (\mathbf{P}_{\mathrm{R}_u}^{-1}\mathbf{Q}_{\mathrm{R}_u}\otimes\mathbf{I}\otimes\mathbf{B})\mathbf{v}^{\mathrm{R}_u} + (\mathbf{I}\otimes\mathbf{P}_{\mathrm{R}_u}^{-1}\mathbf{Q}_{\mathrm{R}_u}\otimes\mathbf{C})\mathbf{v}^{\mathrm{R}_u} + (\mathbf{I}\otimes\mathbf{I}\otimes\mathbf{D})\mathbf{v}^{\mathrm{R}_u} \\
&\quad= \tau_{\mathrm{R}_u}(\mathbf{P}_{\mathrm{R}_u}^{-1}\otimes\mathbf{I}\otimes\boldsymbol{\Sigma}_{\mathrm{R}_u}^{\tau})\left[(\mathbf{e}_1^{\mathrm{R}_u}(\mathbf{e}_1^{\mathrm{R}_u})^{\intercal}\otimes\mathbf{I}\otimes\mathbf{I})\mathbf{v}^{\mathrm{R}_u} - (\mathbf{e}_1^{\mathrm{R}_u}(\mathbf{e}_{m_x}^{\mathrm{L}})^{\intercal}\otimes\mathbf{I}_{\mathrm{L}}^{\mathrm{R}_u}\otimes\mathbf{I})\mathbf{v}^{\mathrm{L}}\right] \\
&\qquad+ \eta_{\mathrm{R}_u}(\mathbf{I}\otimes\mathbf{P}_{\mathrm{R}_u}^{-1}\otimes\boldsymbol{\Sigma}_{\mathrm{R}_u}^{\eta})\left[(\mathbf{I}\otimes\mathbf{e}_1^{\mathrm{R}_u}(\mathbf{e}_1^{\mathrm{R}_u})^{\intercal}\otimes\mathbf{I})\mathbf{v}^{\mathrm{R}_u} - (\mathbf{I}\otimes\mathbf{e}_1^{\mathrm{R}_u}(\mathbf{e}_{m_y}^{\mathrm{R}_\ell})^{\intercal}\otimes\mathbf{I})\mathbf{v}^{\mathrm{R}_\ell}\right],
\end{aligned}
$$

$$
\begin{aligned}
&(\mathbf{I}\otimes\mathbf{I}\otimes\mathbf{M})\mathbf{v}_t^{\mathrm{R}_\ell} + (\mathbf{P}_{\mathrm{R}_\ell}^{-1}\mathbf{Q}_{\mathrm{R}_\ell}\otimes\mathbf{I}\otimes\mathbf{B})\mathbf{v}^{\mathrm{R}_\ell} + (\mathbf{I}\otimes\mathbf{P}_{\mathrm{R}_\ell}^{-1}\mathbf{Q}_{\mathrm{R}_\ell}\otimes\mathbf{C})\mathbf{v}^{\mathrm{R}_\ell} + (\mathbf{I}\otimes\mathbf{I}\otimes\mathbf{D})\mathbf{v}^{\mathrm{R}_\ell} \\
&\quad= \tau_{\mathrm{R}_\ell}(\mathbf{P}_{\mathrm{R}_\ell}^{-1}\otimes\mathbf{I}\otimes\boldsymbol{\Sigma}_{\mathrm{R}_\ell}^{\tau})\left[(\mathbf{e}_1^{\mathrm{R}_\ell}(\mathbf{e}_1^{\mathrm{R}_\ell})^{\intercal}\otimes\mathbf{I}\otimes\mathbf{I})\mathbf{v}^{\mathrm{R}_\ell} - (\mathbf{e}_1^{\mathrm{R}_\ell}(\mathbf{e}_{m_x}^{\mathrm{L}})^{\intercal}\otimes\mathbf{I}_{\mathrm{L}}^{\mathrm{R}_\ell}\otimes\mathbf{I})\mathbf{v}^{\mathrm{L}}\right] \\
&\qquad+ \eta_{\mathrm{R}_\ell}(\mathbf{I}\otimes\mathbf{P}_{\mathrm{R}_\ell}^{-1}\otimes\boldsymbol{\Sigma}_{\mathrm{R}_\ell}^{\eta})\left[(\mathbf{I}\otimes\mathbf{e}_{m_y}^{\mathrm{R}_\ell}(\mathbf{e}_{m_y}^{\mathrm{R}_\ell})^{\intercal}\otimes\mathbf{I})\mathbf{v}^{\mathrm{R}_\ell} - (\mathbf{I}\otimes\mathbf{e}_{m_y}^{\mathrm{R}_\ell}(\mathbf{e}_1^{\mathrm{R}_u})^{\intercal}\otimes\mathbf{I})\mathbf{v}^{\mathrm{R}_u}\right].
\end{aligned}
$$

The coupling terms with τ and η correspond to the couplings at the interfaces with double red lines and double blue lines in Figure 1, respectively. In order to obtain an energy estimate of the semi-discrete numerical scheme (implying time-stability), the parameters are chosen as

$$
\begin{aligned}
&\tau_{\mathrm{L}} = \frac{1}{2}, && \tau_{\mathrm{R}_u} = -\frac{1}{2}, && \tau_{\mathrm{R}_\ell} = -\frac{1}{2}, && \eta_{\mathrm{R}_u} = -\frac{1}{2}, && \eta_{\mathrm{R}_\ell} = \frac{1}{2}, \\
&\boldsymbol{\Sigma}_{\mathrm{L}}^{\tau} = \mathbf{B}, && \boldsymbol{\Sigma}_{\mathrm{R}_u}^{\tau} = \mathbf{B}, && \boldsymbol{\Sigma}_{\mathrm{R}_\ell}^{\tau} = \mathbf{B}, && \boldsymbol{\Sigma}_{\mathrm{R}_u}^{\eta} = \mathbf{C}, && \boldsymbol{\Sigma}_{\mathrm{R}_\ell}^{\eta} = \mathbf{C}.
\end{aligned}
$$

5 NUMERICAL RESULTS

In Sections 5.1 and 5.2 we consider the case $P = 1$, i.e., the deterministic problem, to thoroughly investigate the performance of the presented spatial discretization. Numerical results on the stochastic Galerkin formulation with $P > 1$ is presented in Section 5.3.

5.1 Numerical convergence for the spatial discretization

We carry out a convergence study on the two-level grid in Figures 2(a) and 2(b) using an analytical solution and the method of manufactured solutions to investigate the accuracy of the numerical method [18]. The spatial domain is specified by $L_x = L_y = 300$ m. The analytical solution is given by

$$
E_x(x,y,t) = -E_y(x,y,t) = -376.7H_z(x,y,t) = \cos(\alpha x+\beta)\cdot\cos(\alpha y+\beta)\cdot\cos(\gamma t+\delta), \qquad (7)
$$

with $\alpha = 0.05$, $\beta = 1$, $\gamma = 2\pi/T$, $\delta = -\pi$. The final time is $T = 8\cdot 10^{-4}$ and the parameter values $\epsilon = \mu = 2\cdot 10^{-5}$, $\sigma = 0.1$ are used. The analytical solution (7) solves equation (3) by adding an appropriate right hand side to (3) .

The relative ℓ_2 errors are computed component-wise

$$
\varepsilon_{\ell_2}^{(i)} = \|\mathbf{v}^{(i)} - \mathbf{u}^{(i)}\|_2/\|\mathbf{u}^{(i)}\|_2, \quad i = E_x, E_y, H_z.
$$

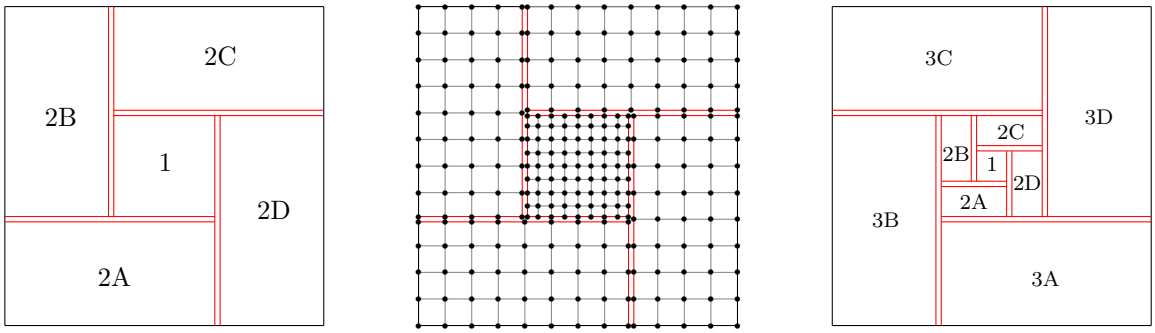

(a) Five grid blocks on two levels of discretization.

(b) Schematic image of grid points for grid in Figure 2(a).

(c) Nine grid blocks on three levels of discretization.

Figure 2: Multi-block grids used in the numerical experiments. All interfaces are of T-junction type.

The discrete ℓ_2 norm over all the spatial blocks is given by

$$\|\mathbf{u}^{(i)}\|_2 = \sqrt{\sum_k \Delta x_k \Delta y_k \sum_{n=1}^{N_k} |\mathbf{u}_{k,n}^{(i)}|^2}, \quad k = 1, 2a, 2b, 2c, 2d,$$

where N_k is the total number of grid points in block k. Let $\mathbf{u}_k^{(i)}$ denote the vector with the exact solution projected on block k and $\mathbf{v}_k^{(i)}$ the vector with the numerical solution on block k, respectively, both for component i. Assuming the same refinement factor c in both dimensions, the numerical convergence rate, $q^{(i)}$, is computed as

$$q^{(i)} = \log(\varepsilon_{\ell_2,c\Delta x}^{(i)} / \varepsilon_{\ell_2,\Delta x}^{(i)}) / \log(c).$$

The ℓ_2 errors and convergence rates are shown in Table 1. Accuracy analysis for the full multi-block discretization is highly non-trivial. The obtained convergence rates of order three are the best one could hope for according to one-dimensional accuracy analysis [19].

$\Delta x, \Delta y$	$\varepsilon_{\ell_2}^{(E_x)}$	$q^{(E_x)}$	$\varepsilon_{\ell_2}^{(E_y)}$	$q^{(E_y)}$	$\varepsilon_{\ell_2}^{(H_z)}$	$q^{(H_z)}$
10	$1.10 \cdot 10^{-3}$		$1.05 \cdot 10^{-3}$		$4.91 \cdot 10^{-1}$	
		3.37		3.34		3.48
5	$1.07 \cdot 10^{-4}$		$1.04 \cdot 10^{-4}$		$4.40 \cdot 10^{-2}$	
		3.25		3.24		3.19
2.5	$1.12 \cdot 10^{-5}$		$1.10 \cdot 10^{-5}$		$4.81 \cdot 10^{-3}$	
		3.00		2.99		3.09
1.25	$1.40 \cdot 10^{-6}$		$1.38 \cdot 10^{-6}$		$5.64 \cdot 10^{-4}$	
		3.22		3.22		3.04
0.625	$1.51 \cdot 10^{-7}$		$1.49 \cdot 10^{-7}$		$6.84 \cdot 10^{-5}$	

Table 1: Numerical convergence for the deterministic problem with two levels, $T = 8 \cdot 10^{-4}$. ℓ_2 error (ε) and order of convergence (q). The grid size refers to the grids on level 2.

5.2 Efficiency of block-decomposed grids

We investigate the efficiency of using the block-decomposed grid depicted in Figure 2(c) compared to uniform grids. The spatial domain is specified by $L_x = L_y = 900$ m, and $\epsilon = \mu =$

$2 \cdot 10^{-5}$, $\sigma = 0.1$. The ratio of grid sizes is 1:2 between levels, and the finest grid is on level 1. We use the initial condition

$$E_x(x, y, t) = -E_y(x, y, t) = -376.7H_z(x, y, t) = e^{-10^{-2}((x-450)^2+(y-450)^2)}.$$

Figure 3 shows the solution at time $T = 0.0048$ computed on the three-level grid depicted in Figure 2(c). Table 2 shows the ℓ_2 errors for the three-level grid and two uniform grids compared to a numerical reference solution computed on a fine uniform grid. Using the three-level grid leads to smaller errors compared to using the uniform grid with equivalent number of degrees of freedom. Errors of the same order of magnitude as for the three-level grid are obtained for a uniform grid with almost twice as many degrees of freedom.

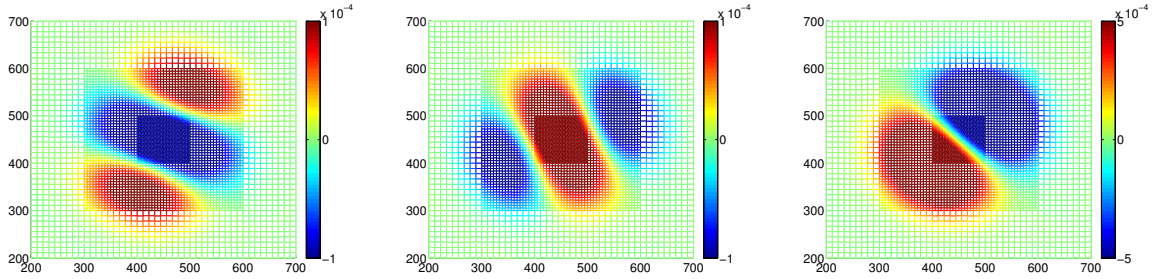

(a) E_x. (b) E_y. (c) H_z.

Figure 3: Solution on three-level grid at time $T = 0.0048$.

total no. of grid points		$\varepsilon_{\ell_2}^{(E_x)}$	$\varepsilon_{\ell_2}^{(E_y)}$	$\varepsilon_{\ell_2}^{(H_z)}$
multi-block grid:	10341	$3.62 \cdot 10^{-3}$	$5.01 \cdot 10^{-3}$	$9.59 \cdot 10^{-4}$
uniform grids:	10404	$1.85 \cdot 10^{-2}$	$1.85 \cdot 10^{-2}$	$1.49 \cdot 10^{-2}$
	19881	$5.93 \cdot 10^{-3}$	$5.93 \cdot 10^{-3}$	$5.75 \cdot 10^{-3}$

Table 2: Numerical convergence for the deterministic problem with three levels, $T = 0.0048$. ℓ_2 errors (ε) for the three-level grid and two uniform grids.

5.3 Convergence of the stochastic Galerkin solution

We now turn to the full stochastic Galerkin system and investigate the performance of different P on the three-level grid in Figure 2(c). We use a lognormal distribution of σ with mean 0.5 and standard deviation 0.2, parameterized with standard Gaussian ξ and Hermite polynomials. The same initial condition as in Section 5.2 is used for the first gPC coefficient and zero for the rest. Mean value and standard deviation of $\mathbf{E}_x$ for $P = 6$ are shown in Figure 4.

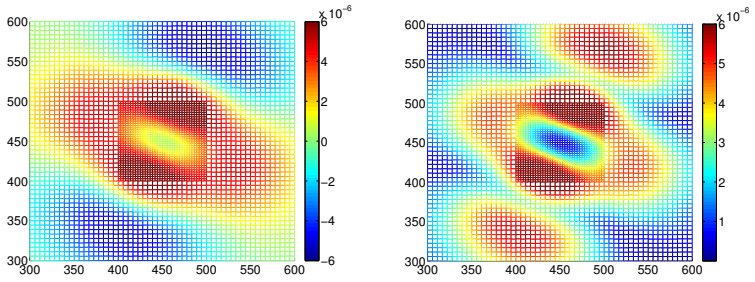

(a) Mean value for $P = 6$. (b) Standard deviation for $P = 6$.

Figure 4: Statistics for $\mathbf{E}_x$ on three-level grid at time $T = 0.012$. Only levels 1 and 2 are shown.

We measure the ℓ_2 norm of the root mean square (RMS) error of the solution

$$\varepsilon_{\ell_2,\mathrm{RMS}} = \frac{\left\| \mathrm{RMS}\left(\mathbf{v}^{(k)} - \mathbf{v}_{\mathrm{ref}}^{(k)}\right)\right\|_2}{\left\| \mathrm{RMS}\left(\mathbf{v}_{\mathrm{ref}}^{(k)}\right)\right\|_2}, \quad \text{where} \quad \mathrm{RMS}(\mathbf{v}_{i,j}^{(k)}) = \sqrt{\mathbb{E}\left[(\mathbf{v}_{i,j}^{(k)})^2\right]} = \sqrt{\sum_{m=1}^{P_{\mathrm{ref}}} \left((\mathbf{v}_{i,j}^{(k)})_m\right)^2}.$$

The ℓ_2 norms of the RMS errors are shown in Table 3. The errors are approximately halved with every increment of P.

P	$\varepsilon_{\ell_2,\mathrm{RMS}}^{(E_x)}$	$\varepsilon_{\ell_2,\mathrm{RMS}}^{(E_y)}$	$\varepsilon_{\ell_2,\mathrm{RMS}}^{(H_z)}$
2	$1.52 \cdot 10^{-1}$	$1.51 \cdot 10^{-1}$	$9.59 \cdot 10^{-2}$
3	$6.77 \cdot 10^{-2}$	$6.74 \cdot 10^{-2}$	$3.64 \cdot 10^{-2}$
4	$3.35 \cdot 10^{-2}$	$3.34 \cdot 10^{-2}$	$1.71 \cdot 10^{-2}$
5	$1.56 \cdot 10^{-2}$	$1.55 \cdot 10^{-2}$	$7.56 \cdot 10^{-3}$
6	$8.32 \cdot 10^{-3}$	$8.27 \cdot 10^{-3}$	$3.79 \cdot 10^{-3}$

Table 3: Discrete ℓ_2 norm in space of RMS errors for different orders P of gPC expansion.

The solution of the stochastic Galerkin Maxwell's equation can be used as a fast surrogate method for sampling in the inverse EM problem. It is essential that the resulting surrogate method represents a probability density function (PDF) that closely resembles the true PDF of the stochastic solution of Maxwell's equations. To quantify this resemblance, we use the Kullback-Leibler divergence, defined for a reference PDF p_{ref} and an estimated PDF p as

$$D_{\mathrm{KL}}(p_{\mathrm{ref}}||p) = \int_{-\infty}^{\infty} \log\left(\frac{p_{\mathrm{ref}}(x)}{p(x)}\right) p_{\mathrm{ref}}(x)\mathrm{d}x. \tag{8}$$

This measure quantifies the amount of information lost when p_{ref} is approximated by p and is equal to zero if the two PDFs are identical. We compute the pointwise in space Kullback-Leibler divergence by first estimating the PDF from the computed gPC coefficients of $\mathbf{v}$ through kernel density estimation methods, assuming a Gaussian kernel. The integral in (8) is then computed

with the trapezoidal rule. Figure 5 depicts the logarithms (base 10) of the Kullback-Leibler divergence for $P = 2, 4, 6$ with respect to a reference PDF generated from the $P = 10$ order gPC expansion. The errors in the PDF estimates are clearly reduced as P increases, but are still quite substantial in some spatial regions. Note that the middle region with the finest grid captures well the PDFs already for $P = 4$. Further investigation is needed to fully evaluate the potential of stochastic Galerkin PDF estimates in geophysical inverse models.

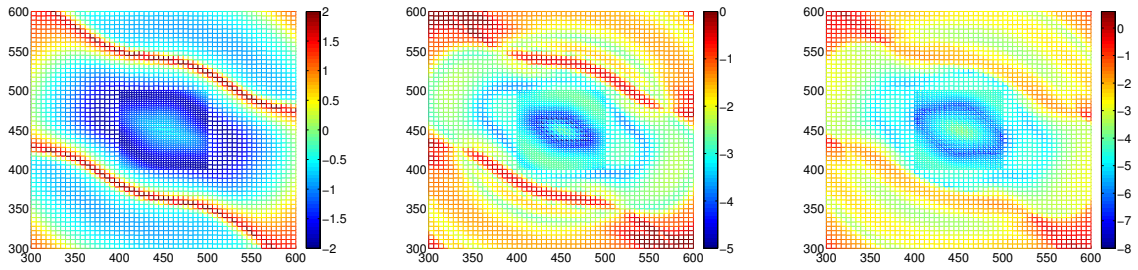

(a) $P = 2$. (b) $P = 4$. (c) $P = 6$.

Figure 5: Logarithm of Kullback-Leibler divergence for $\mathbf{E}_x$ on three-level grid at time $T = 0.012$. Only levels 1 and 2 are shown. Note the different ranges of the color bars.

6 CONCLUSIONS

A time-stable finite difference method for Maxwell's equations has been presented. The proposed method uses the summation-by-parts-operators framework, previously applied to Maxwell's equations on equidistant grids and in this work extended to a stochastic Galerkin formulation and with stable couplings of grid blocks of different grid sizes. This leads to a highly efficient method where regions with high resolution requirements can be sufficiently resolved without the need for excessively fine resolution in the far-field.

We demonstrate third order numerical convergence in space of the method for a deterministic setup on a block-decomposed grids with different grid sizes. In a stochastic setting with lognormal conductivity, the method is evaluated on a block-decomposed grid in terms of convergence with increasing order of gPC expansion. The capabilities of capturing the PDF of the solution is verified by estimating the Kullback-Leibler divergence pointwise in space.

ACKNOWLEDGEMENTS

This work was supported by VISTA (Project 6357) and the SUCCESS Centre for CO_2 storage under grant 193825/S60 from the Research Council of Norway.

REFERENCES

[1] Borcea, L. Electrical impedance tomography. *Inverse Probl.* (2002) **18**(6), R99–R136.

[2] Zhdanov, M. S. Electromagnetic geophysics: Notes from the past and the road ahead. *Geophysics* (2010) **75**(5), 75A49.

[3] Bhuyian, A. H., Landrø, M., and Johansen, S. E. 3D CSEM modeling and time-lapse sensitivity analysis for subsurface CO_2 storage. *Geophysics* (2012) **77**(5), E343.

[4] Gilks, W. R., Richardson, S., and Spiegelhalter, D. J. *Markov Chain Monte Carlo in Practice*. CRC press (1996).

[5] Ghanem, R. and Spanos, P., *Stochastic finite elements: a spectral approach*. Springer, New York (1991).

[6] Xiu, D. and Karniadakis, G. E. The Wiener-Askey polynomial chaos for stochastic differential equations. *SIAM J. Sci. Comput.* (2002) **24**(2):619–644.

[7] Börner, R.-U. Numerical modelling in geo-electromagnetics: advances and challenges. *Surv. Geophys.* (2009) **31**(2), 225–245.

[8] Avdeev, D. B. Three-dimensional electromagnetic modelling and inversion from theory to application. *Surv. Geophys.* (2005) **26**(6), 767–799.

[9] Key, K. and Ovall, J. A parallel goal-oriented adaptive finite element method for 2.5-D electromagnetic modelling. *Geophys. J. Int.* (2011) **186**(1), 137–154.

[10] Commer, M. and Newman, G. A parallel finite-difference approach for 3D transient electromagnetic modeling with galvanic sources. *Geophysics* (2004) **69**(5), 1192–1202.

[11] Svärd, M. and Nordström, J. Review of summation-by-parts schemes for initial-boundary-value problems, *J. Comput. Phys.* (2014) **268**:17–38.

[12] Nissen, A. Kormann, K. Grandin, M and Virta, K. Stable difference methods for block-oriented adaptive grids, *J. Sci. Comput.* (2015) **65**:486–511.

[13] Kreiss, H.-O., and Scherer, G. *Finite element and finite difference methods for hyperbolic partial differential equations*. In Mathematical Aspects of Finite Elements in Partial Differential Equations, pages 179–183. Academic Press, New York (1974).

[14] Carpenter, M. H., Gottlieb, D., and Abarbanel, S. Time-stable boundary conditions for finite-difference schemes solving hyperbolic systems: methodology and application to high-order compact schemes. *J. Comput. Phys.* (1994) **111**(2):220–236.

[15] Strand, B. Summation by parts for finite difference approximations for d/dx. *J. Comput. Phys.* (1994) **110**(1):47–67.

[16] Nordström, J. and Gustafsson, R. High order finite difference approximations of electromagnetic wave propagation close to material discontinuities. *J. Sci. Comput.* (2003) **18**(2), 215–234.

[17] Mattsson, K. and Carpenter, M. H. Stable and accurate interpolation operators for high-order multiblock finite difference methods. *SIAM J. Sci. Comput.* (2010) **32**:2298–2320.

[18] Roache, P.J. Verification of codes and calculations. *AIAA J.* (1988) **36**(5):696–702.

[19] Gustafsson, B., The convergence rate for difference approximations to mixed initial boundary value problems. *Math. Comp.* (1975) **29**:396–406.